Identification of Cracking Mechanisms in Scaled FRP Reinforced Concrete Beams using Acoustic Emission

M.K. ElBatanouny · A. Larosche · P. Mazzoleni ·
P.H. Ziehl · F. Matta · E. Zappa

M.K. ElBatanouny · A. Larosche · P.H. Ziehl (✉) · F. Matta
University of South Carolina, 300 Main Street,
Columbia, SC 29208, USA
e-mail: ziehl@cec.sc.edu

M.K. ElBatanouny
e-mail: elbatano@email.sc.edu

A. Larosche
e-mail: a.larosche@gmail.com

F. Matta
e-mail: fmatta@sc.edu

P. Mazzoleni · E. Zappa
Politecnico di Milano, via La Masa, 1,
Milan 20156, Italy

P. Mazzoleni
e-mail: paolo2.mazzoleni@mail.polimi.it

E. Zappa
e-mail: emanuele.zappa@mecc.polimi.it

Introduction

The use of corrosion resistant glass fiber reinforced polymer (GFRP) reinforcement in lieu of steel bars is an attractive option for non-prestressed concrete structures that operate in aggressive environments, such as bridges, parking garages, seawalls and docks [1]. Design principles that reflect the peculiar properties of GFRP reinforcement, including its rel-atively low stiffness and linear elastic behavior in uniaxial tension up to failure, are fairly well established. Guideline documents [2] followed by codes of practice [3, 4] and mate-rials and construction specifications [5, 6] have been pub-lished in the last decade and are available to practitioners. The lower axial stiffness of GFRP bars, as compared to steel, results in wider cracks reducing the depth of the uncracked concrete in compression and hindering aggregate interlock along the inclined (shear) cracks, thereby reducing shear strength [7, 8]. In addition, size effect, which is defined as the decrease in shear stress at failure at increasing effective depths of the cross section, becomes more of concern [9–11]. In concrete beams, cracks are typically classified as flex-ural cracks and shear cracks. Flexural cracks generally occur due to the presence of direct tensile stresses that exceed the tensile strength of the concrete. Shear cracks occur due to a combination of tensile and shear stresses where the principal

tensile stress exceeds the tensile strength of the concrete. Under a typical four-point bending setup, flexural cracks develop primarily in the constant moment region (between the loading sections), whereas shear cracks develop in the constant shear regions (between either loading section and the adjacent support) in the form of inclined fractures that grow towards either loading section. As a shear crack grows, sliding may occur at the crack interface causing friction between the crack surfaces, and shear force may be transferred via aggregate interlock along the irregular interface. Given the difference in the mechanism of flexural and shear cracks, it is postulated that each crack type may be associated with different characteristics of the transient stress waves that are released.

Acoustic emission (AE) consists of transient stress waves (in the kHz range) emitted as a result of sudden energy release, such as cracks or friction [12–14]. The sensitivity of AE sensors to these high frequency ranges enables the detection of micro-cracks prior to the visual observation of the macro-cracks resulting from the coalescence of micro-cracks. AE is primarily used as a passive monitoring tool for structures made of reinforced and prestressed concrete, fiber reinforced polymer (FRP) composites (e.g. bridge decks and pressure vessels), and steel. Standard test procedures have been developed for quantifying damage in FRP tanks and vessels [15, 16]. Several AE studies have focused on both the quantification of damage and structural health monitoring purposes [17–19].

This study investigates the sensitivity of AE for the determination of crack type. The results are intended to improve the criteria and methodologies to validate assumptions associated with failure analyses in terms of crack development and mechanisms. Five scaled GFRP RC beams without shear reinforcement were tested under four-point bending. Acoustic emission was used to investigate the cracking mechanism. AE features enabled to discrimination between different crack types (flexural and shear) and recognition of impending failure regardless of the failure mode.

Research Significance

The mechanics of crack development in concrete structures is not well defined with conventional instrumentation. The sensitivity of acoustic emission was exploited to investigate and describe the differences in the AE signatures associated with the mechanisms of flexural and shear cracks that developed in GFRP RC beams with scaled effective depth and maximum aggregate size. The ability to characterize cracking mechanisms is instrumental to understand the mechanics of crack development and failure [20], including the much debated role of aggregate interlock as the primary shear force transfer mechanism and source of size effect [21, 22]. From a more practical standpoint, the implementation of this knowledge into structural health monitoring and prognosis systems will enable recognition of whether a structure is nearing a brittle and thus catastrophic failure (such as shear failure of a RC beam without shear reinforcement).

This study aims to contribute to the definition of rational criteria for the classification of crack type in large scale specimens. The number of sensors used for AE data analysis along with the data filtering techniques implemented can be adapted to field testing of actual structures.

Specimens and Materials

Five scaled GFRP RC beams were cast. The beams were divided into groups of large and small scale specimens that included two and three beams, respectively, as summarized in Table 1. Schematics of the cross sections are showed in Fig. 1. The smaller scale specimens, herein denoted as GS1, GS2 and GS3, were constructed with a length, l, width, b_w, and depth, h, of 2440, 230, and 180 mm, respectively. The effective depth of the GFRP reinforcement, d, was 145 mm. The larger scale specimens herein denoted as GM1 and GM2 had a length, width, and depth of 3350, 115, and 330 mm, respectively. The effective depth of the GFRP reinforcement was 290 mm, thus scaled up by a factor of 2 with respect to that of the GS specimens.

The average concrete compressive strength, f_c', for each specimen was determined per ASTM C39 at the time of testing and is reported in Table 1. A maximum aggregate size, a_g, of 13 mm was used except for specimen GS3, where a_g was also scaled by a factor of 1/2 to 6 mm with respect to its larger scale counterparts.

Table 1 Specimens geometry and relevant material properties

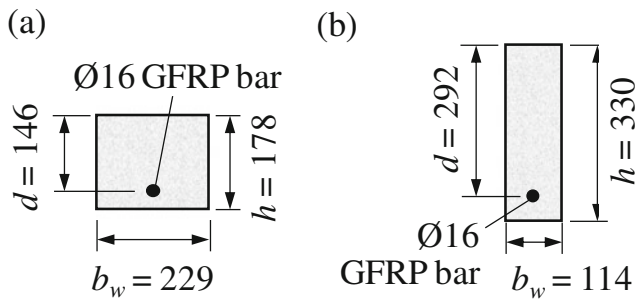| Specimen name	b_w (mm)	D	a	a/d	m (mm)	l	f_c' (MPa)	a_g (mm)	E_f (GPa)
GS1	229	146	457	3.1	305	610	41.1	13	49.3
GS2							40.8		
GS3							46.8	6	
GM1	114	292	914	3.1	305	610	40.1	13	49.3
GM2							41.6		

Fig. 1 Cross section of GFRP RC beam specimens: (**a**) smaller scale, GS and (**b**) larger scale, GM (dimensions in mm)

Each specimen was reinforced in the longitudinal direction with a single Ø16 mm pultruded E-glass/vinyl ester GFRP bar, resulting in an effective reinforcement ratio (ρ_{eff}; given by the ratio of the cross sectional area of the reinforcement to that of the effective cross section, $b_w d$, multiplied by the ratio of the elastic modulus of the GFRP to that of steel) of 0.15 %, which is a lower bound that is representative of real-case scenarios. The average longitudinal elastic modulus, E_f, and average ultimate strength, f_{fu}, of the GFRP bars was 49.3 GPa and 785 MPa, respectively, as determined per ASTM D7205. The specimens did not include any shear reinforcement and are thus scaled representations of a strip of a slab bridge, deck or retaining wall (both wall and foundation slab).

The four-point bending test setup is illustrated in Fig. 2. Table 1 summarizes the length of the shear span, a, the length of the constant moment region, m, and the anchorage length of the GFRP bars past the supports, l. For all beams, a constant shear span-to-depth ratio, a/d, of 3.1 was used to minimize arching action, thus yielding conservative values of strength [23]. The load was imparted by means using hydraulic actuators and measured with load cells. The specimens were instrumented with strain gauges to measure deformations in the
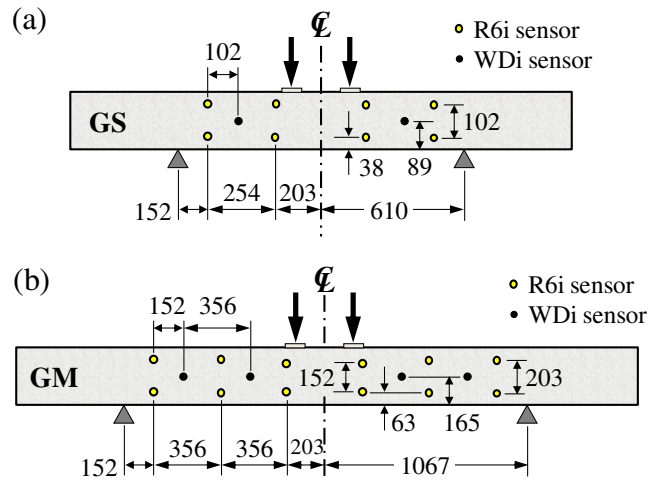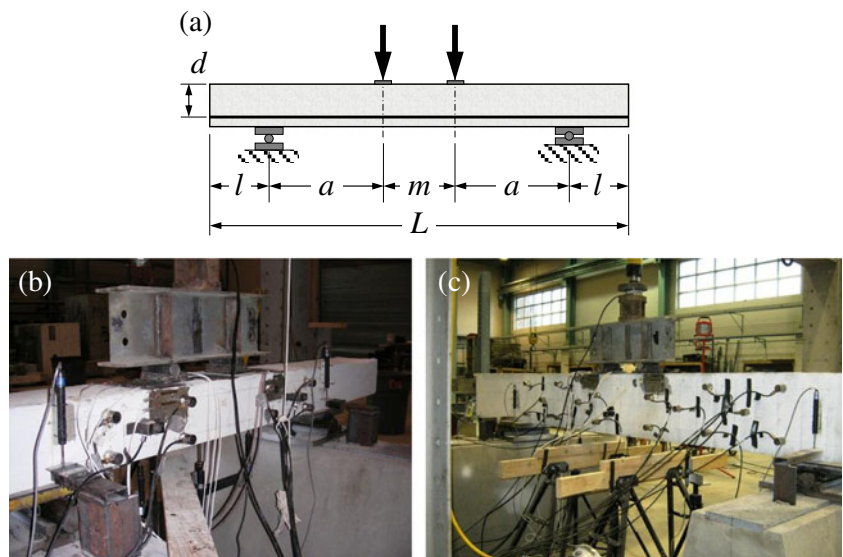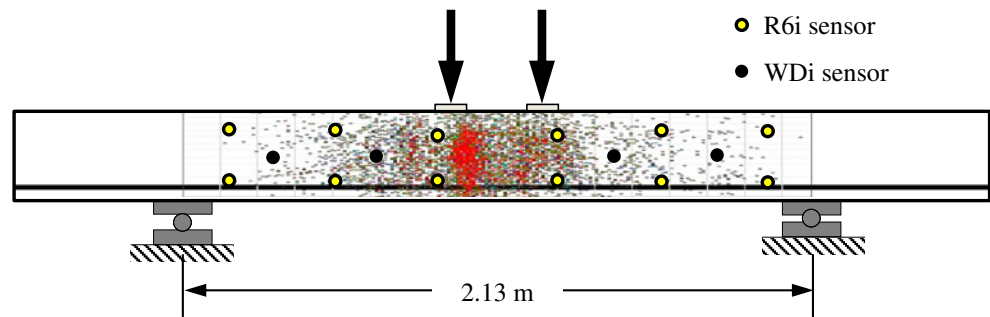

Fig. 3 AE sensor layout: (**a**) GS specimens, and (**b**) GM specimens (dimensions in mm)

GFRP reinforcement and the concrete, and with displacement transducers to measure vertical displacements.

Acoustic Emission

Acoustic emission sensors were mounted on each specimen. The surface of the specimens was first cleaned and a two part epoxy was used to attach the sensors. Pencil lead breaks were used to determine wave speed and to check the attenuation associated with each sensor according to ASTM E1316 [14]. Two types of AE sensors were used: resonant sensors in the vicinity of the 55 kHz (R6i), and wide band sensors (WDi), each constructed with an integral 40 dB preamplifier. An array of 10 AE sensors was mounted on the small scale (GS) specimens, including eight resonant and two wide band sensors. The number of AE sensors

Fig. 2 Load test setup: (**a**) schematic, (**b**) photograph of GS specimen setup, and (**c**) photograph of GM specimen setup

Fig. 4 Crack locations in specimen GM1 using unfiltered AE data

2.13 m

R6i sensor
WDi sensor

was increased to 16 for the medium scale (GM) specimens, including 12 resonant and four wide band sensors. The AE sensor layouts for each specimen size are shown in Fig. 3. The resonant sensors were intended primarily for source location whereas the wide band sensors were intended primarily for crack classification.

AE Data Filtering

Acoustic emission data was collected using a 16-channel data acquisition system (Sensor Highway II, Mistras Group, Inc.). The AE amplitude threshold was set at 50 dB for all specimens. Raw AE data contain emissions generated from noise, wave reflections as well as friction between the loading apparatus and the concrete surface. General laboratory conditions have been closely monitored to ensure the absence of electromagnetic noise. Friction was minimized by inserting neoprene pads between the loading plates and the concrete surface. The hit lockout time (HLT) was set to 1000 µs in an effort to reduce reflections as the reflected wave will have to travel a distance of at least 3 m before it is recorded. Given the attenuation of AE signals in concrete along with the travel distance and specimen size, the reflected wave will be diminished. Reflections occurring at time intervals smaller than the hit definition time (HDT) will merge with the real signal causing long duration signals. Since the elimination of false emissions, wave reflections and friction between the loading apparatus and the concrete surface is not possible, filtering of the AE data was a critical task. To illustrate this point, Fig. 4 shows the result of source

location from a representative beam specimen test (GM1) utilizing unfiltered AE data.

Proper filtering of AE data can be accomplished using waveform analysis performed for individual hits. Although this method is the most effective, when large amounts of data are present the time needed to perform the analysis becomes unpractical. As such, the AE data from these tests were filtered using amplitude and waveform-based filters. The amplitude filter level was chosen such that noise was minimized while retaining data pertinent to the results of the test. The waveform based filters are combinations of data having particular duration-amplitude characteristics, and are referred to as D-A filters (Swansong II filters). These filters were developed based on the observation that waveforms associated with noise generally have relatively low amplitude and high duration. The D-A filters were previously implemented for filtering data from full-scale specimens and are suitable for being applied to both laboratory and field data [24, 25]. The D-A filters therefore exclude data having particular amplitude and duration characteristics and were developed based on visual inspection of waveforms. The same filters were applied to all specimens to enable comparison. Both filter limits are shown in Table 2.

Waveform Based Parameters

Each AE hit comprises a large number of parameters that can be calculated from its waveform including, but not limited to: amplitude, duration, rise time, average frequency,

Table 2 Rejection limits for data filters

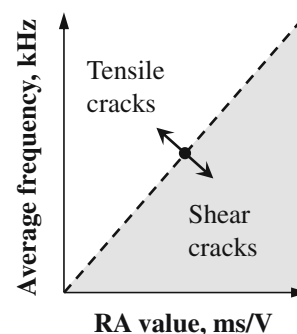| Filter type	Amplitude (dB)	Duration (µs)
Amplitude	< 60	–
Duration-amplitude	60-67	>2,000
	68-75	>4,000
	76-83	>6,000
	84-91	> 8,000
	92-100	>10,000

Fig. 5 Schematic of crack classification based on relation between average frequency and RA value

Table 3 Summary of test results

Specimen	Loads (kN)		Failure mode
	Failure load, V_{exp}	Nominal flexural load[a], V_f	
GS1	44.2	43.8	Flexure (GFRP bar rupture)
GS2	46.0	43.8	
GS3	25.2	45.9	Shear (diagonal tension)
GM1	22.7	43.4	
GM2	17.8	44.0	

[a]Theoretical load associated with nominal bending moment

peak frequency, counts, RMS (root mean square of voltages in the AE waveform), and signal strength (definitions provided in 'AE terminology'). Most of these parameters have been previously investigated for the determination of damage in concrete structures [16–18]. However, limited research has been performed on the nature of the AE waveform signature associated with different types of cracks [20, 26–31]. This study focuses on AE parameters of amplitude, peak frequency (PFrq), and rise time for classification of crack types.

Existing Crack Classification Methods

At least two methods have been proposed for the classification of cracks: average frequency versus RA value and moment tensor analysis [26–31]. The first method is parameter based and uses rise time, maximum amplitude, counts, and duration to calculate two indices: RA value and average frequency as shown in equations (1) and (2). It has been reported that tensile cracks tend to have low RA value and high average frequency while shear cracks tend to follow the opposite trend. The

proportional limit for this empirical relation has not yet been fully determined [27]. The relationship hypothesis is shown in Fig. 5.

$$\text{RA (in ms/V)} = \text{Rise time(in } \mu s)/\text{Maximum amplitude(in mV)} \tag{1}$$

$$\text{Average frequency} = \text{Counts/Duration(in ms)} \tag{2}$$

Moment tensor analysis can be used to determine crack locations and orientations [28]. The method classifies cracks quantitatively in three categories; (2) tensile cracks, (b) shear cracks, and (c) mixed mode cracks. This method is carried out based on arrival time and amplitude of the first motion. The method is not easily implemented in field tests as it requires at least six sensors located at three different planes in the vicinity of a known crack or expected crack location. A study has recently been conducted to classify cracks using both of the listed methods with the results of each being compared. Good results were achieved from the parameter based method, however the events were first located and determined based on a moment tensor analysis

Fig. 6 Photographs of representative beams after failure: (a-b) specimen GS1 (GFRP bar rupture), (c) GS3 (*shear failure*), and (d) GM1 (*shear failure*)
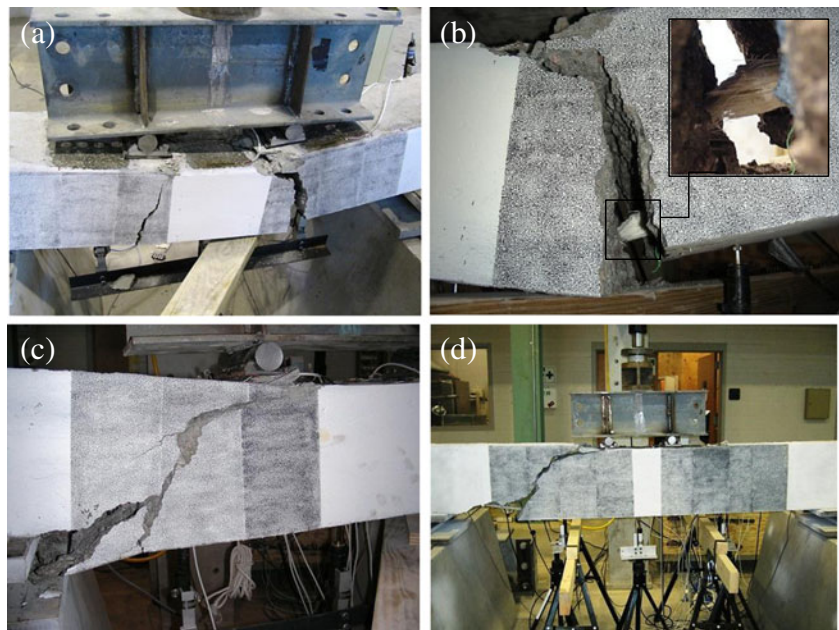
[28]. The sensor layout utilized in this study is not sufficiently dense to reliably perform a moment tensor analysis.

Parameter based analysis with limited amount of sensors was also used to characterize fracture process. Results showed that AE parameters during and after crack formations are different from AE parameters prior to cracking [30, 31]. Additionally, most of the specimens used in the literature measured $100 \times 100 \times 400$ mm [28, 30, 31]. The work presented herein deals with large scale specimens. In specimens such as these cracks are visible after the occurrence of the first flexural crack. As the load is increased, additional flexural and shear cracks develop. Therefore classification methods implemented in previous studies may not be applicable in this study.

Results and Discussion

Failure Mode

Table 3 summarizes the experimental shear force in the shear span at failure, V_{exp}, the nominal force associated with flexural failure, V_f, computed per the ACI 440.1R-06 guidelines [2], and the failure mode. The contribution of self-weight at a distance d from the loading section is accounted for, assuming a concrete density of 2,320 kg/m^3.

SpecimensGS1 and GS2 failed due to a flexural crack developing until the FRP strain reached the ultimate value, leading to the rupture of the GFRP bar [Fig. 6(a-b)] at a load similar to the nominal value, V_f (Table 3). The remaining beams failed in shear. In particular, in the case of specimen GS3, the scaling of the maximum aggregate size from 13 mm to 6 mm led to a shift in the failure mode from rupture of the GFRP bar (flexural failure in GS1 and GS2) to shear failure, as shown in Fig. 6(c), consistent with the behavior of the larger scale (GM) counterparts, as shown for GM1 in Fig. 6(d).

From a practical standpoint, it is noted that experimental evidence from small scale specimens where the maximum aggregate size is not scaled may be very misleading if the results were extrapolated to large scale specimens having similar maximum aggregate size. More details regarding the size effect in GFRP reinforced concrete beams can be found in Matta et al. [9, 11].

Crack Mapping

Results related to crack mapping are presented for representative scaled specimens that failed in shear (GS3 and GM1). The AE source location technique was used to generate crack maps. The method is similar to that used to determine the epicenter of an earthquake, and relies on the difference in the arrival time of recorded hits for different AE sensors to determine the location

of a given AE source using the wave speed. Two-dimensional AE source location was performed since all the sensors were mounted on one side of the specimen.

For specimen GM1, the load history was divided into four stages as shown in Fig. 7(a). A nonlinear behavior due to the decrease in flexural stiffness following the opening of the first flexural crack was observed in Stage 2 as shown in Fig. 7(b). Figure 8 illustrates the crack development at the different load stages. Visually observed cracks were plotted using high resolution photographs taken at various times and load levels as shown in Fig. 9. The AE activity is plotted with visually observed cracks following a particular loading phase presented with a black line. In Stage 1, flexural cracking is observed near the center line of the beam. In Stage 2, additional flexural cracks are detected. AE activity was also detected at the right side of the beam centered near a space approximately 560 mm away from the centerline of the beam. In Stage 3 the inclined shear crack at the right side began to grow. Additional AE activity was detected in the
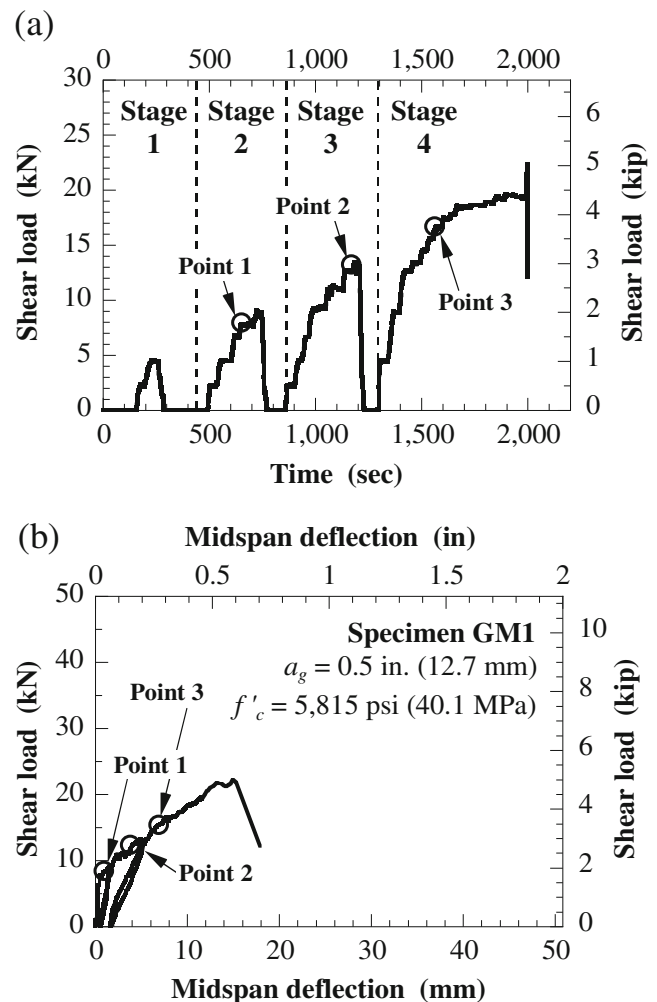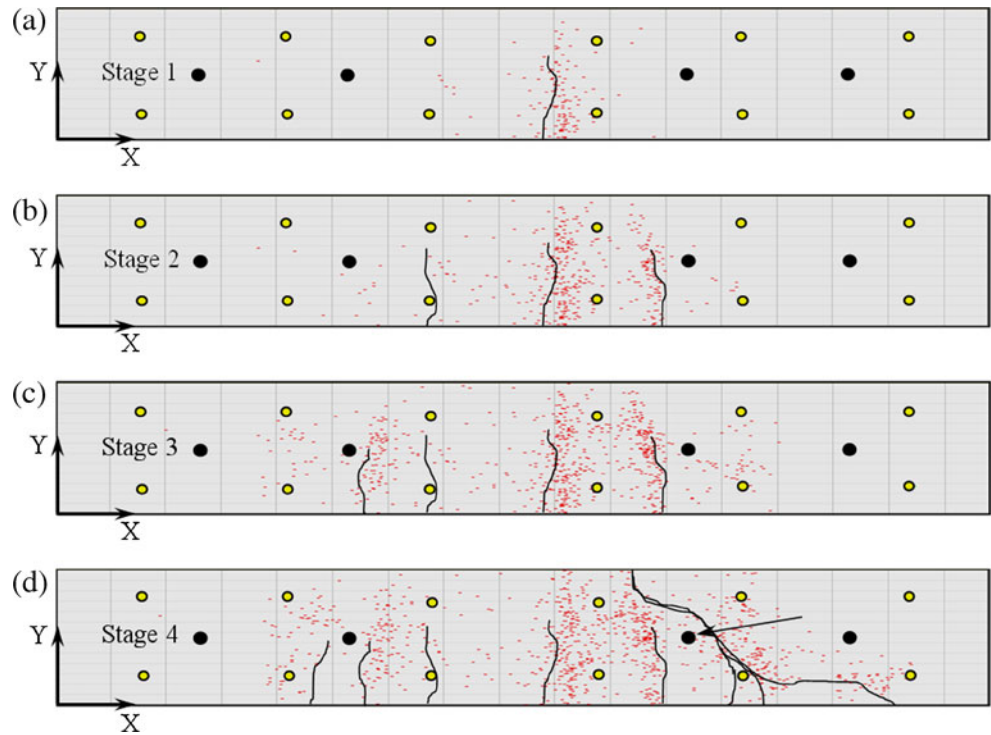

Fig. 7 Specimen GM1: (a) load history, and (b) load-deflection response

Fig. 8 Crack development in specimen GM1 during load stages: (**a**) Stage 1, (**b**) Stage 2; (**c**) Stage 3, and (**d**) Stage 4. Arrow in (**d**) shows AE sensor chosen for crack classification data (Plots are not to scale. Only area between supports is shown)

proximity of the inclined crack, which was also observed through visual inspection. In Stage 4 AE events continued to increase in the area where the inclined crack was propagating. The location of these events together with the progressive increase in applied load indicate that the AE events are associated with friction and aggregate interlock along the interface of the inclined crack.

A similar analysis was performed for specimen GS3 as shown in Fig. 10. The load-deflection curve for GS3 is shown in Fig. 11(b). The load history was divided into four stages. Only flexural cracks developed during stage 1, 2, and 3. In Stage 4, the critical shear (inclined) crack that will lead to failure initiated at the right side of the specimen.

Another shear crack started to grow at the left side of the specimen. The shear crack at the right side propagated into the uncracked concrete above the neutral axis, rapidly leading to a brittle (sudden) failure. From Fig. 11(b), it can be seen that during the propagation of the shear crack in Stage 4 no increase in the load was observed.

Crack Classification

The load-deflection curves for specimen GS1 and GS3 in Fig. 11 show that the behavior of the two specimens deviated at a specific bifurcation area at a shear load of about 25 kN. At this load, the critical shear crack in GS3 rapidly

Fig. 9 Photographs with marked cracks in specimen GM1: (**a**) area covered by camera, (**b**) Stage 3, (**c**) prior to peak load, and (**d**) after peak load
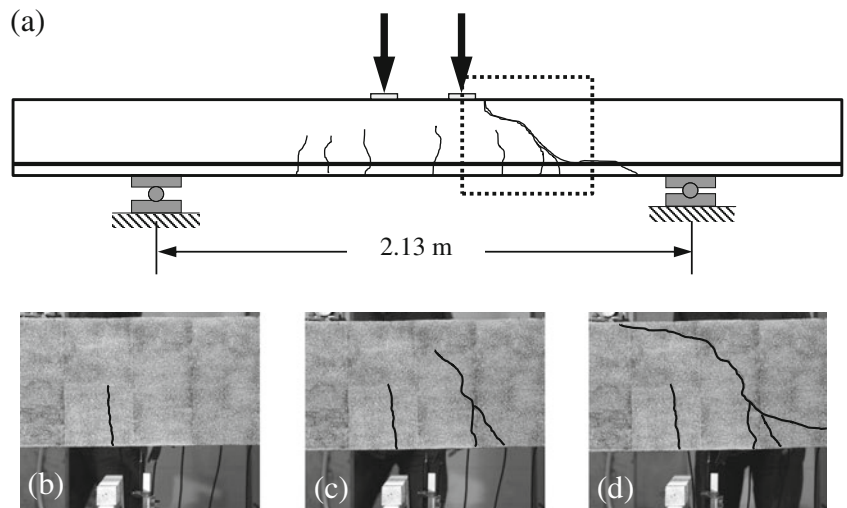
Fig. 10 Crack development in specimen GS3 during load stages: (**a**) Stage 1, (**b**) Stage 2; (**c**) Stage 3, and (**d**) Stage 4. Arrow in (**d**) shows AE sensor chosen for crack classification data (Plots are not to scale. Only area between supports is shown)
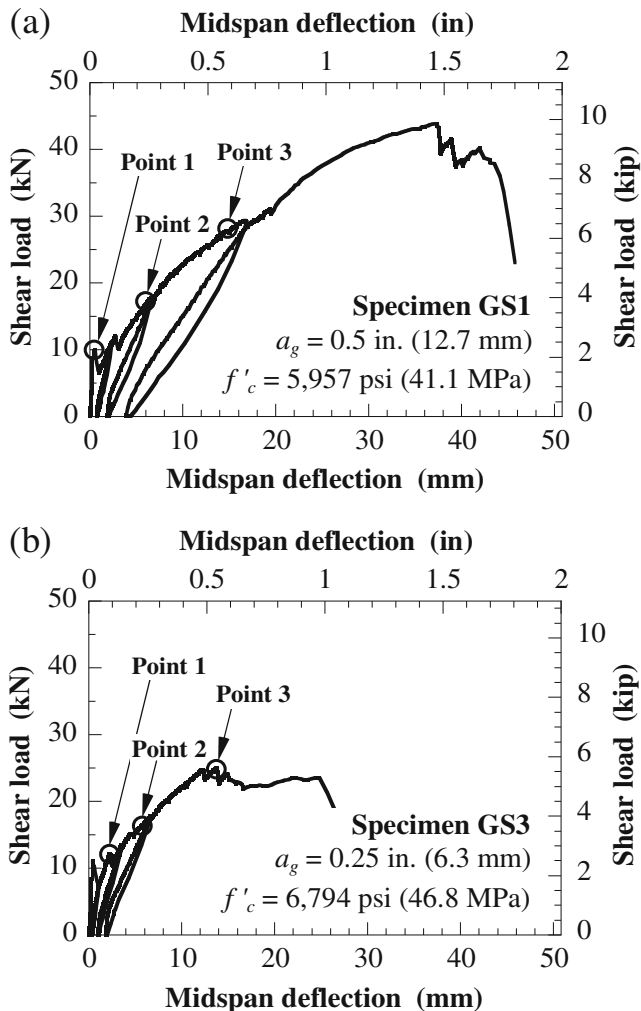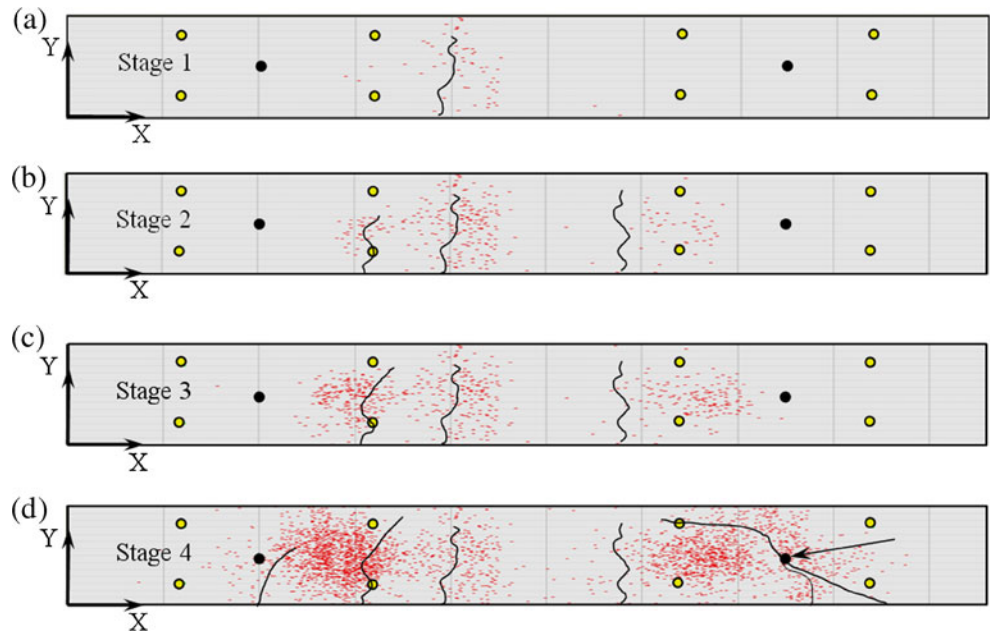

Fig. 11 Load versus deflection: (**a**) GS1, and (**b**) GS3. Arrows indicate load–displacement region for selected points for analysis

developed and led to brittle shear failure without noticeable increases in the load. Conversely, the load increased in specimen GS1 until flexural failure occurred due to rupture of the GFRP bar. A similar behavior was observed in GS3's larger scale counterpart GM1 as shown in Figs. 6(d) and 7 (b). The AE waveform parameters were analyzed for AE signatures associated with each cracking mechanism. The data acquired through the wide band sensors located in the vicinity of the crack locations (within 250 mm from the source) of interest were used as shown in Figs. 8 and 10. This was done to reduce the effect of the source-to-sensor distance and to ensure the absence of cracks in the path between signals and sensors. Only wide band sensors were used for this purpose since they have a wider frequency range compared with the resonant sensors, and can therefore acquire signals closer to their original frequency [30]. All hits recorded by the selected wide band sensors, shown in Figs. 8 and 10, were used in the analysis

Three points in the load history of specimen GM1 were chosen such that during the first two points only flexural cracking occurred. The third point was chosen for the representation of shear cracking. The crack types at these points were verified using high resolution pictures taken at various times and load levels. Cross plots of peak frequency (PFrq) versus AE amplitude are plotted at each of the three points as shown in Fig. 12(a). The AE signature associated with flexural cracks consistently differs from that of shear cracks. At flexural cracking points, two clusters of AE data appear at peak frequencies of 50 kHz and 100 kHz. The average peak frequency at both points was less than 80 kHz. At the point of shear cracking peak frequency was clustered at an average value of 97.5 kHz with a significantly lower standard deviation (10.8 compared to 29.8 and 29.3 for flexural cracking).
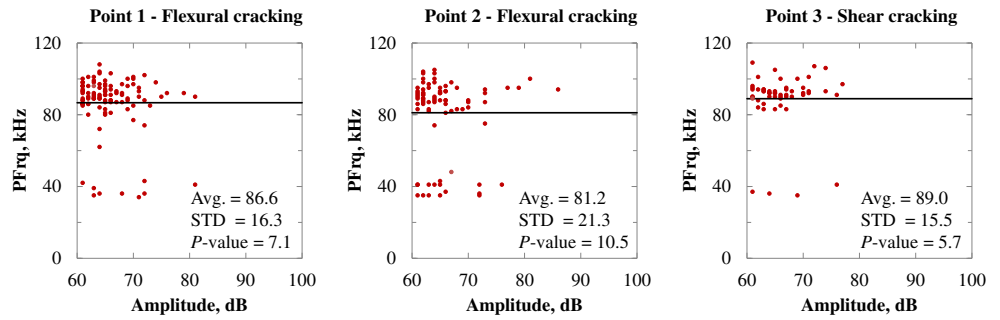
Fig. 12 Cross plots of AE amplitude and peak frequency (PFrq): specimen (**a**) GM1, (**b**) GS1 and (**c**) GS3
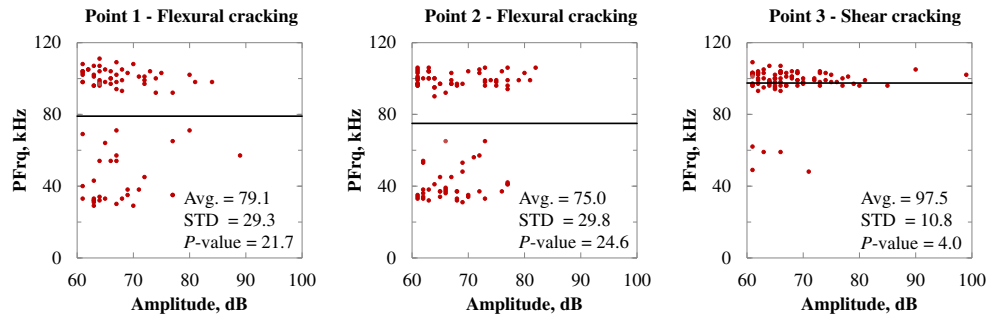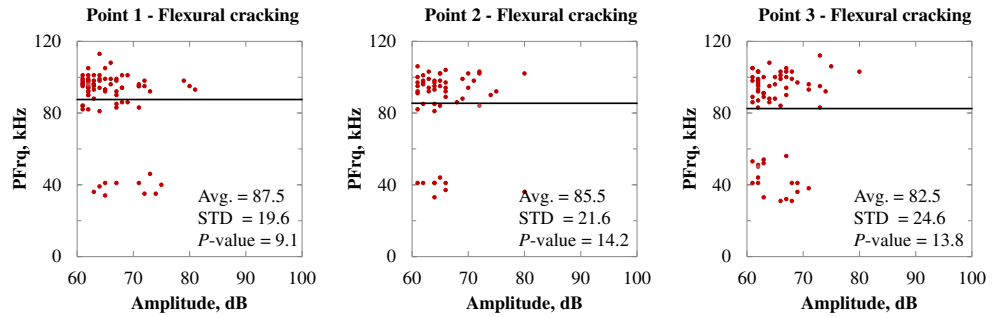
(a) GM1: larger scale, 13 mm maximum aggregate size

(b) GS1: smaller scale, 13 mm maximum aggregate size

(c) GS3: smaller scale, 6 mm maximum aggregate size

Three points (short intervals) in the load history of small scale specimens GS1 and GS3 were chosen (Fig. 11(a) and (b), respectively) and a similar analysis was performed. The time duration of these points as well as the number of hits and crack type are shown in Table 4. Specimen GS1 failed in flexure without formation of shear cracks. This behavior was reflected in the cross-plots where no increase in the average peak frequency occurred [Fig. 12(b)]. In the case of specimen GS3, shear cracks formed at Point 3 in the load history [Fig. 11(b)]. This specimen had a trend similar to that of its larger scale counterpart GM1, which also failed in shear, where the peak frequency formed two clusters when flexural cracking was taking place at Point 1 and 2, while the peak frequency clustered at a higher average value when shear cracking took place.

The peak frequency data was further analyzed by calculating P-value for each data set in Fig. 12. The P-value is defined as the difference between the centroid of the peak frequencies above the average peak frequency and the value of the average

peak frequency. For the GM1 data sets, a significant difference in the P-value was found between AE waves (hits) associated with flexural cracking and shear cracking hits. The P-values for specimen GS1, especially points 2 and 3, were relatively similar as the specimen did not exhibit shear cracking [Fig. 12(b)]. In specimen GS3, the difference in P-value between flexural cracking hits and shear crack hits is less significant when compared to specimen GM1. For flexural cracking, the P-value ranged from 7.1 to 24.6 while for shear cracking the P-value ranged from 4.0 to 5.7. Therefore a limit for the P-value may be set at 7 to distinguish between shear and flexural cracking where values smaller than 7 are indicative of shear cracking and values greater than 7 are indicative of flexural cracking.

The results point to the potential for the use of peak frequency as a damage descriptor in relation to the crack type. This parameter was independent of specimen size. Amplitude distribution did not vary considerably for the different loading stages and specimens; however higher AE amplitude events

Table 4 Summary of properties of chosen points for analysis

Specimen	Point 1			Point 2			Point 3		
	Duration (s)	Hits	Crack type	Duration (s)	Hits	Crack type	Duration (s)	Hits	Crack type
GM1	50	79	F	50	96	F	50	90	S
GS1	70	78	F	90	53	F	100	66	F
GS3	50	107	F	100	80	F	70	55	S

were recorded for the shear cracking stage of specimen GM1 than for the other specimens and stages.

The AE waveforms for the three selected points in each specimen were further analyzed. Cross plots of rise time versus amplitude were compared to investigate differences between flexural and shear cracks as shown in Fig. 13. For specimen GS3, when shear cracking took place a significant decrease in rise time occurred when compared to the rise time associated with flexural cracking. It is also noticed that the data are more clustered when shear cracks took place, with an associated drop in standard deviation. No significant differences were noticed from the plots for specimen GS1 (only flexural cracking occurred in this specimen). The average rise time decreased slightly toward the end of the test; however no clustering was seen in the data.

The analyses of the AE data after the bifurcation point in both specimens indicates that shear cracks were developing in specimen GS3 while flexural cracking was observed in specimen GS1. This is reflected in plots for GS1—point 3 and GS3—point 3 in Figs. 12 and 13.

Damage Detection

The acoustic emission method is well known for its ability to detect distributed damage in different materials [17] and is a potential candidate for use during load testing to preclude collapse [32, 33]. To investigate this potential, AE waveform based analysis was performed on hits recorded prior to failure. Figure 14 shows cross plots for RMS (root mean square of voltages in the AE waveform) versus AE amplitude at Point 1 and 2 and prior to failure (Point 3) in specimens GM1, GS1, and GS3. RMS increases by one order of magnitude prior to failure, and provides a promising means to recognize impending failures. Of particular interest, this phenomenon was observed in AE data recorded with either the wide band or the resonant sensors and was independent of specimen size and failure mode.
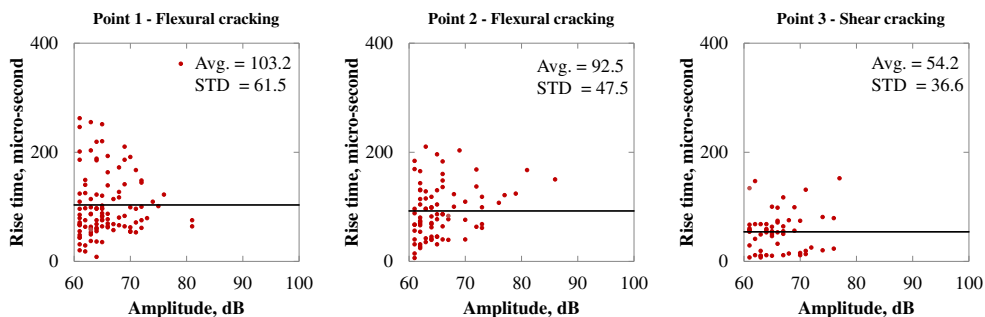
b-value Analysis

The *b*-value analysis is based on a seismological magnitude-frequency relation that was developed by Gutenberg and

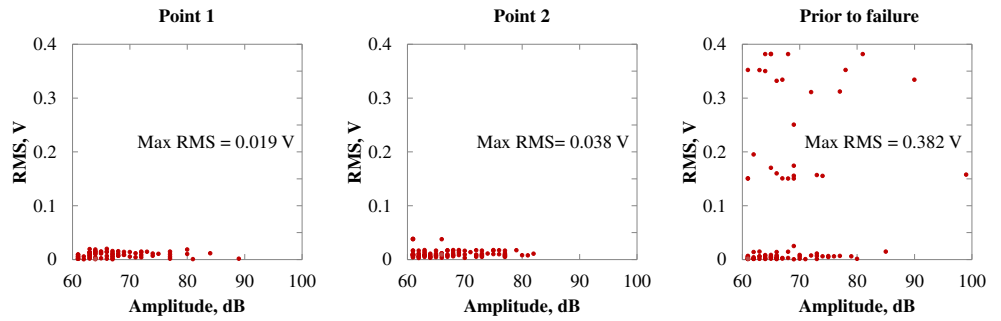**Fig. 13** Cross plots of AE amplitude and rise time: specimen (**a**) GS1 and (**b**) GS3
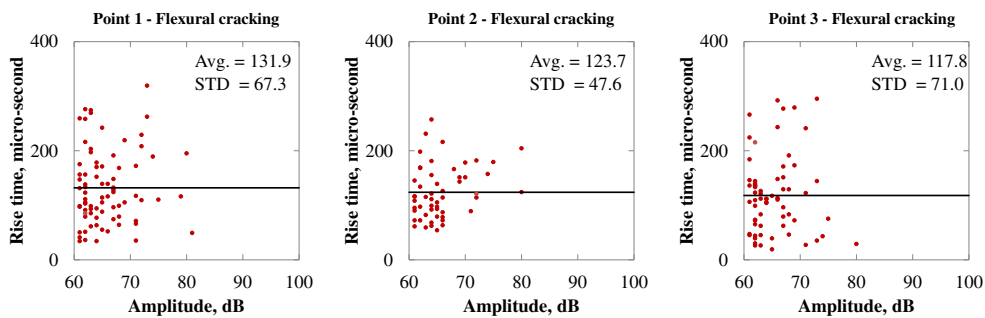
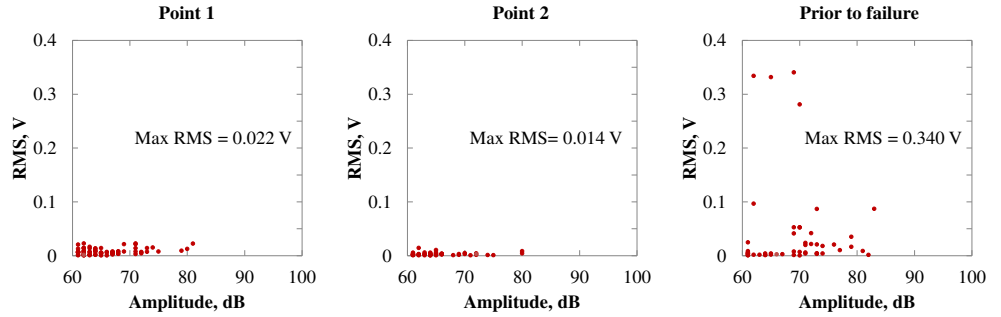(a) GS1: smaller scale, 13 mm maximum aggregate size
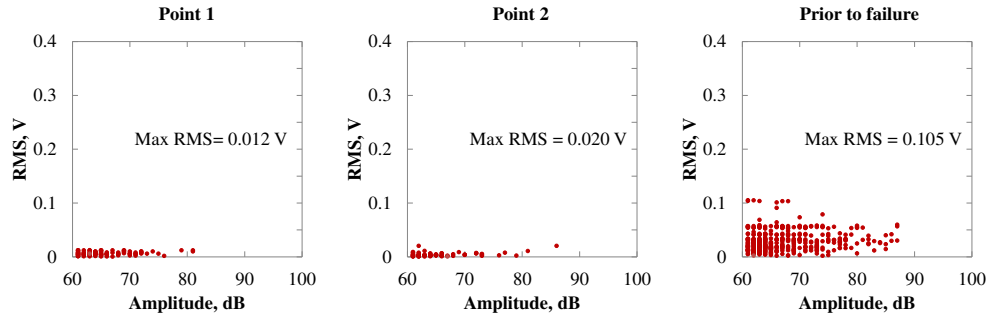
(b) GS3: smaller scale, 6 mm maximum aggregate size

Fig. 14 Cross plots of AE amplitude and RMS: specimen (**a**) GM1, (**b**) GS1 and (**c**) GS3

(a) GM1: larger scale, 13 mm maximum aggregate size

(b) GS1: smaller scale, 13 mm maximum aggregate size

(c) GS3: smaller scale, 6 mm maximum aggregate size

Richter [34] to describe the fact that events of larger magnitude occur less frequently than those of smaller magnitude. This method calculates the frequency of earthquake magnitudes occurring during a certain period of time. The *b*-value has been adopted in acoustic emission analysis in the area of rock mechanics and was applied to concrete

Fig. 15 *b*-value analysis for specimen GS2
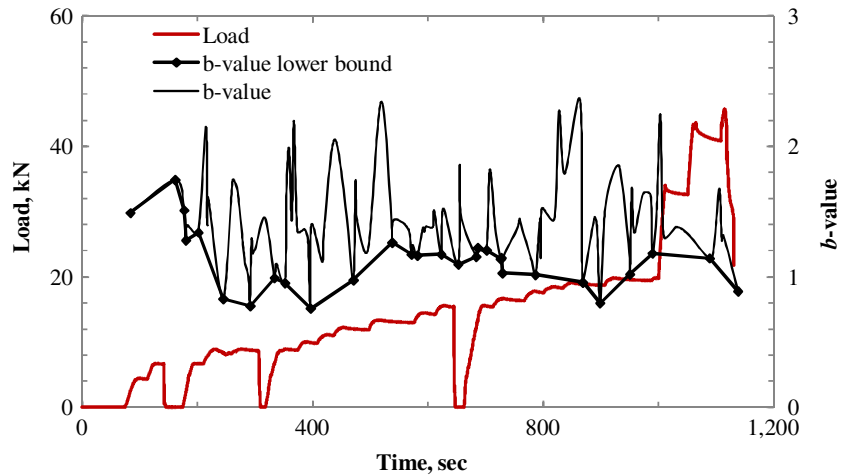
structures [17, 31, 35–38]. The relation used for *b*-value analysis is shown in equation (3):

$$\log N = a - b \log A \tag{3}$$

where: N is the number of hits with amplitudes greater than A, A is the amplitude in dB, a is an empirical constant, and b is the *b*-value. The concept of the method is to measure the frequency of the magnitude of hits and relate it to cracking. This can be related to cracking by considering that micro (non-visible) cracks release low amplitude AE hits, whereas and macro (visible) cracks release high amplitude AE hits. Therefore a lower *b*-value will contain higher numbers of large amplitude hits and serves as an indication that macro-cracks are forming; i.e. major damage has occurred. It has been reported that *b*-values below 1.0 indicate that a macro-crack has taken place [17].

The *b*-value analysis works as a sliding window. For specimen GS2, 50 AE hits were used to calculate a single *b*-value [31, 37]. The number of hits included in the b-value analysis is dependent on the amount of data collected and the type of test. The *b*-value as compared to load for specimen GS2 was calculated as shown in Fig. 15. The loading protocol consisted of four load cycles increasing in magnitude from 6.7 to 45.9 kN. The rate of loading also varied between cycles since the load was imparted using a manually-operated hydraulic jack. The formation of cracks increases the attenuation in AE signal which in turn may increase the *b*-value between the drops. Therefore, in order to better visualize the relevant data, the local minimum values attained by the *b*-value during the test are also indicated in Fig. 15. The *b*-value decreases to 0.77 after the opening of the first crack at 290 s, which is in agreement with previous studies [17, 31].

Conclusions

The conclusions of this study are summarized as follows:

1. Experimental evidence from small scale specimens where the maximum aggregate size is not scaled may be misleading both in terms of strength and failure mode, when used to validate the design of larger members without shear reinforcement.
2. Acoustic emission has the ability to locate cracking provided that proper filters are applied to minimize noise and reflections in the AE dataset.
3. Differences in the AE signature associated with flexural cracks and shear cracks were found. The peak frequency tends to increase and cluster when shear cracks are present. This finding was verified from other specimens with different size which indicates that the parameter may be independent of size. Flexural and shear cracks

were also identified in small scale specimens based on the AE rise time.
4. The RMS enabled recognition of impending failure of the specimens regardless of size, failure mode, and sensor type.
5. *b*-value analysis likewise enabled recognition of impending failure during the load test.

It is noted that using AE to discriminate crack type in specimens with relatively large size is challenging. In such specimens multiple cracks typically develop prior to failure which leads to a constant change in the source to sensor distance. Furthermore the attenuation increases as a result of deterioration in the specimen. Also cracks developed in the source-to-sensor path may prevent the AE waves from reaching the sensors or at least get distorted. Nevertheless, results from tests on large-size specimens are more applicable to the field testing of actual structures.

The results achieved from this study, as well as similar previous studies, are based on experiments. Understanding and modeling the underlying physics from different crack sources is an important topic for further investigation. The classification methods discussed in this study are empirical. Future work should investigate the effects of source-to-sensor distance on the parameters used for classification of cracks [39] Appendix.

Appendix A

Relevant terminology related to Acoustic Emission [40]

Each of the below listed parameters were calculated and given by the data acquisition program.

Amplitude: The largest voltage peak in the AE signal waveform; customarily expressed in decibels relative to 1 µV at the preamplifier input (dB) assuming a 40 dB preamp.

dB: A unit of measurement for AE signal amplitude A, defined by $A\ (dB) = 20\ log\ V_p$; where V_p is the peak signal voltage in µV referred to the preamplifier input.

Duration: The time from the first threshold crossing to the end of the last threshold crossing of the AE signal from the AE threshold.

Signal Strength: The measured area of the rectified AE signal with units proportional to volt seconds (the proportionality constant is specified by the AE instrument manufacturer).

Rise time: The time from an AE signal's first threshold crossing to its peak.

Counts: The number of times the AE signal crosses the detection threshold.

Peak Frequency: The point in the power spectrum at which the peak magnitude occurs. The peak frequency is a 2 byte value reported in kHz.

RMS: The root mean square is a measure of continuous varying AE voltage. It is defined as the rectified time averaged AE signal measured on a linear scale and reported in volts.

RA value: The ratio between rise time and maximum amplitude in Volts from an AE signal.

References

1. Matta F (2008) Industry/University Cooperative Research on Advanced Composite Reinforcement for Concrete: Translating Innovation into Sustainable Engineering Practice. Proc. NSF International Workshop on the Use of Fiber Reinforced Polymers for Sustainable Structures, Cairo, Egypt, May 22, CD-ROM, pp 13

2. American Concrete Institute (ACI) Committee 440 (2006) Guide for the Design and Construction of Structural Concrete Reinforced with FRP Bars—ACI 440.1R-06. ACI, Farmington Hills, MI

3. Canadian Standards Association (CSA) (2006) Canadian highway bridge design code—CAN/CSA-S6-06. CSA, Mississauga

4. American Association of State Highway and Transportation Officials (AASHTO) (2009) AASHTO LRFD bridge design guide specifications for GFRP-reinforced concrete bridge decks and traffic railings, 1st edn. AASHTO, Washington

5. American Concrete Institute (ACI) Committee 440 (2008) Specification for carbon and glass fiber-reinforced polymer bar materials for concrete reinforcement—ACI 440.6-08. ACI, Farmington Hills, MI

6. American Concrete Institute (ACI) Committee 440 (2008) Specification for construction with fiber-reinforced polymer reinforcing bars—ACI 440.5-08. ACI, Farmington Hills, MI

7. Gross SP, Yost JR, Dinehart DW, Svensen E, Liu N (2003) Shear Strength of Normal and High Strength Concrete Beams Reinforced with GFRP Bars. ASCE Special Publication: Proceedings of the International Conference on High Performance Materials in Bridges and Buildings, Kona, Hawaii, pp 426–437

8. Tureyen AK, Frosch RJ (2003) Concrete shear strength: another perspective. ACI Structural Journal 100(5):609–615

9. Matta F, Mazzoleni P, Zappa E, Sutton A, ElBatanouny M, Larosche A, Ziehl P (2012) Shear strength of FRP reinforced concrete beams without stirrups: verification of fracture mechanics formulation. ACI Special Publication Spring Convention 2012, Dallas, TX

10. Bentz EC, Massam L, Collins MP (2010) Shear strength of large concrete members with FRP reinforcement. J Compos Construct 14(6):637–646

11. Matta F, El-Sayed AK, Nanni A, Benmokrane B (2012) Size Effect on Concrete Shear Strength in Beams Reinforced with FRP Bars. In press ACI Structural Journal

12. Ziehl P (2008) Applications of acoustic emission evaluation for civil infrastructure. SPIE Smart Structures and Materials and Nondestructive Evaluation and Health Monitoring, San Diego, p 9

13. Pollock AA (1986) Classical Wave Theory in Practical AE Testing. Progress in AE III, Proceedings of the 8th International AE Symposium, Japanese Society for Nondestructive Testing, pp 708–721

14. ASTM E1316 (2006) Standard terminology for nondestructive examinations. American Standard for Testing and Materials, 1–33

15. ASTM E1067/E1067M-11 (2011) Standard practice for acoustic emission examination of Fiberglass Reinforced Plastic Resin (FRP) Tanks/Vessels. American Standard for Testing and Materials, 1–15

16. Fowler T, Blessing J, Conlisk P (1989) New directions in testing. Proc. 3rd International Symposium on AE from Composite Materials, Paris, France

17. Ono, K. (2010) Application of acoustic emission for structure diagnosis. KonferencjaNaukowa, pp. 317–341

18. Golaski L, Gebski P, Ono K (2002) Diagnostics of reinforced concrete by acoustic emission. J Acoust Emi 20:83–98

19. ElBatanouny M, Mangual J, Ziehl P, and Matta F (2011) Corrosion Intensity Classification in Prestressed Concrete using Acoustic Emission Technique. Proc. American Society for Nondestructive Testing (ASNT) Fall Conference and Quality Testing Show 2011, Palm Springs, CA, October 24–28, pp 10

20. Katsaga T, Sherwood EG, Collins MP, Young RP (2007) Acoustic emission imaging of shear failure in large reinforced concrete structures. Int J Fract 148(1):29–45

21. Collins MP, Kutchma D (1999) How safe are our large, lightly reinforced concrete beams, slabs, and footings. ACI Struct J 96 (4):482–490

22. Bažant ZP, Yu Q, Gerstle W, Hanson J, Ju JW (2007) Justification of ACI 446 proposal for updating ACI code provisions for shear design of reinforced concrete beams. ACI Structural Journal, V. 104, No. 5, Sep.-Oct. 2007, pp 601–610

23. Kani GNJ (1967) How safe are our large reinforced concrete beams. ACI J 64(3):128–141

24. Fowler TJ, Blessing JA, Conlisk PJ, Swanson TL (1989) The Monpac system. Journal of Acoustic Emission. 8(3)

25. Tinkey BV, Fowler TJ, Klingner RE (2002) Nondestructive testing of prestressed bridge girders with distributed damage. Res Rep 1857–2:106

26. Shiotani T, Yuyama S, Li ZW, Ohtsu M (2001) Application of the AE improved b-value to qualitative evaluation of fracture process in concrete materials. J Acoust Emi 19:118–132

27. Ohtsu M, Okamoto T, Yuyama S (1998) Moment tensor analysis of acoustic emission for cracking mechanisms in concrete. ACI Structu J 95(2):87–95

28. Ohno K, Ohtsu M (2010) Crack classification in concrete based on acoustic emission. Construct Build Mater 24:2339–2346

29. Ohtsu M, Ono K (1984) A generalized theory of acoustic emission and green's functions in a half space. J Acoust Emi 3(1):124–33

30. Aggelis DG (2011) Classification of crack mode in concrete by using acoustic emission parameters. Mech Res Comm 38:153–157

31. Aggelis DG, Soulioti DV, Sapouridis N, Barkoula NM, Paipetis AS, Matikas TE (2011) Acoustic emission characterization of the fracture process of fiber reinforced concrete. Construct Build Mater 25:4126–4131

32. Liu Z, Ziehl P (2009) Evaluation of RC beam specimens with AE and CLT criteria. ACI Struct J 106(3):1–12

33. Ziehl P, Galati N, Tumialan G, Nanni A (2008) *In-situ* evaluation of two rc slab systems—part II: evaluation criteria. ASCE J Perform Constr Facil 22(4):217–227

34. Gutenberg B, Richter CF (1954) Seismicity of the earth and associated phenomena, 2nd edn. Princeton University Press, Princeton

35. Sammonds PR, Meredith PG, Murrel SAF, Main IG (1994) Modelling the damage evolution in rock containing pore fluid by acoustic emission. Eurock '94, Balkerna, Rotterdam, The Netherlands

36. Cox SJD, Meredith PG (1993) Microcrack formation and material softening in rock measured by monitoring acoustic emission. Int J Rock Mech Min Sci Geomech Abstr 30(1):11–21

37. Shiotani T, Ohtsu M, Ikeda K (2001) Detection and evaluation of AE waves due to rock deformation. Construct Build Mater 15(5–6):235–246

38. Colombo S, Main IG, Forde MC (2003) Assessing damage of reinforced concrete beam using b-value analysis of acoustic emission signals. J Mater Civil Eng 5–6:280–286

39. Aggelis DG, Mpalaskas AC, Ntalakas D, Matikas TE (2012) Effect of wave distortion on acoustic emission characterization of cementitious material. Construct Build Mater 35:183–190

40. Grosse CU, Ohtsu M (2008) Acoustic emission testing. Springer, Berlin